Unusual polarity-dependent patterns in a bent-core nematic liquid crystal under low-frequency ac field

Ying Xiang,[1] Meng-jie Zhou,[1] Ming-Ya Xu,[1] Péter Salamon,[2] Nándor Éber,[2,*] and Ágnes Buka[2]

[1]*School of Information Engineering, Guangdong University of Technology, Guangzhou 510006, People's Republic of China*

[2]*Institute for Solid State Physics and Optics, Wigner Research Centre for Physics, Hungarian Academy of Sciences, H-1121 Budapest, Konkoly Thege Miklós út 29-33, Hungary*

(Received 8 January 2015; published 2 April 2015)

Electric-field-induced patterns of diverse morphology have been observed over a wide frequency range in a recently synthesized bent-core nematic (BCN) liquid crystal. At low frequencies (up to ∼25 Hz), the BCN exhibited unusual polarity-dependent patterns. When the amplitude of the ac field was enhanced, these two time-asymmetrical patterns turned into time-symmetrical prewavylike stripes. At ac frequencies in the middle-frequency range (∼50–3000 Hz), zigzag patterns were detected whose obliqueness varied with the frequency. Finally, if the frequency was increased above 3 kHz, the zigzag pattern was replaced by another, prewavylike pattern, whose threshold voltage depended on the frequency; however, the wave vector did not. For a more complete characterization, material parameters such as elastic constants, dielectric permittivities, and the anisotropy of the diamagnetic susceptibility were also determined.

DOI: 10.1103/PhysRevE.91.042501 PACS number(s): 61.30.−v, 78.20.Jq, 42.70.Df, 47.54.−r

I. INTRODUCTION

Liquid crystals (LCs) being a fluid and ordered medium, when driven by a high enough voltage and current, can undergo electroconvection (EC), which arises from the couplings among the orientation of the LC molecules, the flow of both material and charge, and the applied electric and the space-charge field [1]. EC effects are often manifested in the appearance of various patterns, whose characteristics (such as the onset voltage U_c, the critical wave vector $\mathbf{q}_c$, and the frequency range of existence) are closely related to the electric transport properties of LCs as well as the boundary conditions [2].

Investigation of EC phenomena and exploration of the underlying mechanisms effectively contribute to the better understanding of the behavior and the physical properties of LCs. Thorough experimental studies have been conducted on LC systems formed by rodlike molecules, which explored a multifariousness of pattern morphologies (including normal, oblique, and longitudinal rolls; prewavy, wavy, and two-dimensional grid patterns, etc.) depending on materials and the control parameters (the rms value U and the frequency f of the driving ac voltage). Based on these researches, a standard theoretical model (SM) of EC has been developed describing the essential Carr-Helfrich feedback mechanism and clarifying the role of various material parameters in the pattern formation [3]. The SM can satisfactorily provide the onset characteristics for a group of patterns known at present as "standard EC"; in order to distinguish them from "nonstandard EC" which cannot be interpreted within the framework of the SM and thus needs the inclusion of other phenomena (e.g., flexoelectricity, ionic effects, etc.) [2]. Some nonstandard patterns arise due to flexoelectricity; typically they manifest themselves as longitudinal rolls (i.e., rolls running parallel or slightly oblique to the initial director orientation $\mathbf{n_0}$) [4]. The prewavy (or wide domain) instability is another kind of nonstandard pattern, typically occurring at high f (above a few kHz) and forming stripes normal to $\mathbf{n}_0$ with a wavelength much larger than the sample thickness d [5].

Recently new kinds of LC systems based on bent-core molecules have attracted considerable interest [6]. The bent-core nematics (BCNs) studied so far mostly exhibit various nonstandard EC patterns [7–20], whose characteristics may substantially differ from those in calamitic LCs. Moreover, there are some unprecedented scenarios, like prewavy patterns at ultrahigh ($f > 50$ kHz) frequencies with negative slope of $U_c(f)$, which have been found so far only in BCN compounds [7,11–13]. These banana-specific features still wait for explanation.

Therefore, investigation of EC of BCN systems is a timely task; the experimental results may contribute to uncovering the behavior of BCN materials and may provide a base for future improvement and/or extension of the theoretical description of EC.

It should be noted that traditional investigations on EC effects have mostly been performed in the ac frequency range of about 10 Hz–10 kHz, where the growth and decay times τ of the EC patterns are much larger than the period $t_0 = 1/f$ of the driving ac voltage. This frequency range has recently been extended to ultralow frequencies representing the other limit $\tau \ll t_0$, where pattern evolution within the driving period t_0 could be monitored and even morphological transitions between patterns occurring in different time slots could be detected [21,22].

In the present paper we focus on a symmetric, difluoromethyleneoxy-bridged bent-core LC compound having 1,3,4-oxadiazole as the central ring and explore its EC pattern formation characteristics in a wide frequency range, including ultralow as well as ultrahigh frequencies. We report on distinct pattern morphologies found in three, well defined (low, middle, and high) f ranges. Specifically, at low f the patterns were unexpectedly found to exhibit a pronounced time-asymmetrical, polarity-dependent behavior, appearing alternately in the first and second half cycles of the driving field.

*eber.nandor@wigner.mta.hu

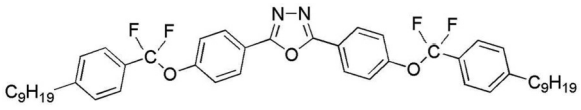

Cr – 87.3 °C – Sm – 91.2 °C – N – 126.4 °C – I

FIG. 1. Structural formula and phase sequence of the 2,5-bis(4-(difluoro(4-nonylphenyl)methoxy)- phenyl)-1,3,4-oxadiazole (9P-CF_2O-ODBP) BCN compound.

The paper is structured as follows. In Sec. II we introduce the studied compound and the setup used during the experiments. Then in Secs. III A–III C we characterize the patterns occurring in the specific frequency ranges. An additional Sec. III D is devoted to the determination of the key material parameters of the BCN compound. Finally, in Sec. IV, we close the paper with a discussion and some concluding remarks.

II. COMPOUND AND EXPERIMENTAL SETUP

Measurements have been performed on the BCN compound 2,5-bis(4-(difluoro(4-nonylphenyl)methoxy)phenyl)-1,3,4-oxadiazole (9P-CF_2O-ODBP). Its structural formula as well as its phase sequence is shown in Fig. 1. The compound exhibits an enantiotropic nematic and a yet unidentified smectic phase. The phase transition temperatures given in Fig. 1 were obtained by differential scanning calorimetry (DSC) in heating. It can be seen that the compound has low melting and clearing points and a wide nematic range, at least compared to other 1,2,3-oxadiazole BCN materials [16,17,23]. The lowering of the temperatures may be related to a possible decrease of intermolecular interactions due to the replacement of the ester bridge by fluorine substituted methoxy groups.

Samples of the BCN compound were filled into standard planar sandwich cells of a $d = 6\,\mu$m thickness. The initial director orientation $\mathbf{n_0}$ along the x axis was provided by antiparallel rubbed polyimide alignment layers [24]. The electric field $\mathbf{E}$ was applied along the z axis, i.e., perpendicular to the substrates and $\mathbf{n_0}$. The temperature of the samples was controlled using a Linkam LTS 350/TMS 94 heating stage with a relative accuracy of 0.01 °C.

A sinusoidal ac voltage of rms value U from a function generator was applied to the cell through a broadband high-voltage amplifier. The EC patterns were observed by a Leica DM RXP polarizing microscope in transmission mode using a single polarizer only (shadowgraph technique), and the images were captured by a controllable frame rate, high-speed digital camera (Mikrotron EoSens MC 1362). Image capturing was synchronized to the zero crossing of the driving ac voltage by a trigger signal of the function generator. The system allowed monitoring of the temporal evolution of the pattern formation by recording a sequence of 100–2000 images within a full period of the driving ac voltage. In order to allow a quantitative comparison of the recorded images, they were digitally processed: the image contrast was defined as the mean square deviation of the pixel intensities. This has a low background value in the initial homogeneous state, and increases as the pattern emerges.

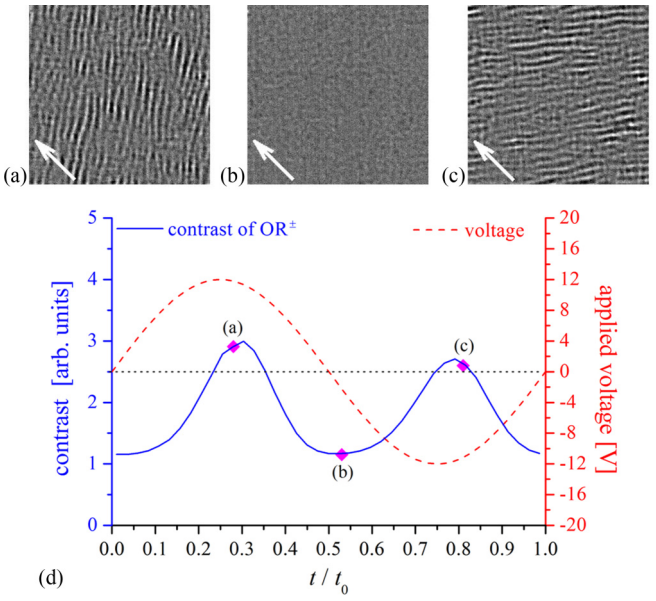

FIG. 2. (Color online) Representative snapshots of the low-frequency ac voltage driven oblique roll pattern. (a) OR^+ near onset in the positive half period; (b) no pattern around the zero crossing of the voltage; (c) OR^- near onset in the negative half period. All snapshots are of 100 μm × 100 μm size. The white arrows indicate the initial director $\mathbf{n_0}$; the polarizer direction is vertical. (d) Temporal dependence of the pattern contrast and of the applied voltage within one full period. The symbols denote the time instants when the snapshots were taken. $f = 12$ Hz, $U = 8.3$ V, $T = 97\,^\circ$C.

III. EXPERIMENTAL RESULTS

The experiments were carried out in the nematic phase of 9P-CF_2O-ODBP at $T = 97.0\,^\circ$C, over a wide frequency and voltage range of the driving ac field, where patterns occurred. In the following the behavior of those patterns is overviewed.

A. The low-frequency range

At low frequencies (below a critical frequency $f_{c1} \approx 25$ Hz) oblique rolls with two distinct directions (OR^+ and OR^-) occur alternatingly within one period of the driving voltage. Representative snapshots are shown in Figs. 2(a) and 2(c), respectively. The roll directions of OR^+ and OR^- are symmetric with respect to $\mathbf{n_0}$; the wave vector of OR^+ in Fig. 2(a) makes an angle $\alpha_{OR^+} \approx 40^\circ$ with $\mathbf{n_0}$, while for OR^- in Fig. 2(c) $\alpha_{OR^-} \approx -40^\circ$. They represent the two degenerate modes of a zigzag pattern. In order to explore the pattern evolution, sequences of snapshots have been taken and their contrast has been determined as a function of time. Figure 2(d) exhibits the temporal evolution of the pattern contrast as well as that of the driving voltage for one full period t_0 at $U = 8.3$ V, $f = 12$ Hz (near onset). It is clearly seen that the contrast has two maxima (one in each half period); between them the contrast falls back to the background level. This indicates the periodic formation [Figs. 2(a) and 2(c)] and decay [Fig. 2(b)] of patterns. Inspection of the snapshots proved that OR^+ always occurs in the positive, and OR^- in the negative half period of the voltage; hence the roll direction is polarity dependent.

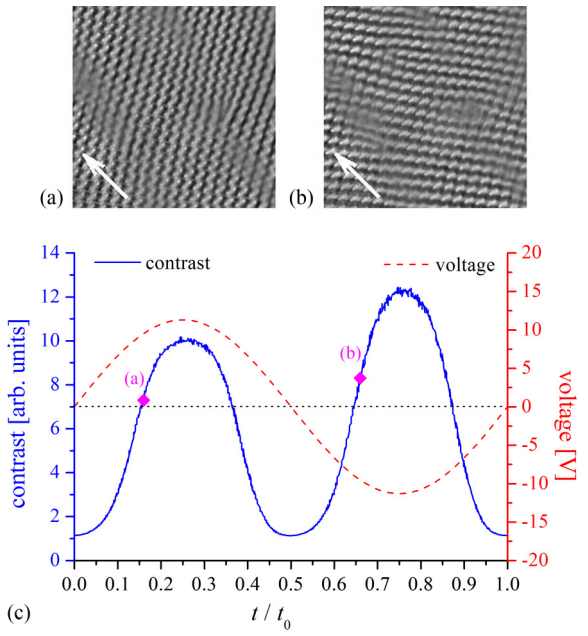

FIG. 3. (Color online) Representative snapshots of the low-frequency ac voltage driven oblique roll pattern. (a) OR^+ in the positive half period; (b) OR^- in the negative half period. Both snapshots are of 100 μm × 100 μm size. The white arrows indicate the initial director $\mathbf{n}_0$, the polarizer direction is vertical. (c) Temporal dependence of the pattern contrast and of the applied voltage within one full period. The symbols denote the time instants when the snapshots were taken. $f = 5$ Hz, $U = 8.0$ V, $T = 97\,^\circ$C.

We point out that the scenario outlined above (i.e., the alternation of OR^+ and OR^-) holds for all f in the low-frequency ($f < f_{c1}$) range. As an illustration Figs. 3(a) and 3(b) show representative snapshots; Fig. 3(c) exhibits the time evolution of the contrast for another combination, $f = 5$ Hz, $U = 8.0$ V, of the control parameters. The larger contrast as well as the undulation of the stripes (a secondary instability) indicates that the sequence of snapshots was taken at a voltage further away from the threshold than those shown in Fig. 2.

The polarity sensitive behavior of the wave vector under ac driving is quite unusual, since EC is typically governed by quadratic (proportional to the amplitude square E^2 of the ac electric field) interactions. Therefore the pattern is expected to be the same in the positive and in the negative half cycle of the applied voltage.

It can be seen from Figs. 2(d) and 3(c) that the contrast maxima follow the peak voltages by some time delay; the contrast is thus phase shifted with respect to the driving voltage. This phase shift is larger at higher frequencies.

One can also notice that the maximal contrast values of OR^- and OR^+ are not identical. This asymmetry we attribute to the presence of a small dc offset voltage (∼±0.3 V) inherent to the high-voltage dc amplifier. Whether OR^+ or OR^- has larger contrast maximum depends on the sign of the offset voltage, which was positive in Fig. 2(d), but negative in Fig. 3(c). A similar effect of the dc offset is known for standard EC and flexodomains too; moreover, in the case of flexodomains it could even be calculated theoretically [21].

The voltage U_{OR}, which represents the threshold for OR^+ and OR^-, increases nearly linearly with the frequency, except

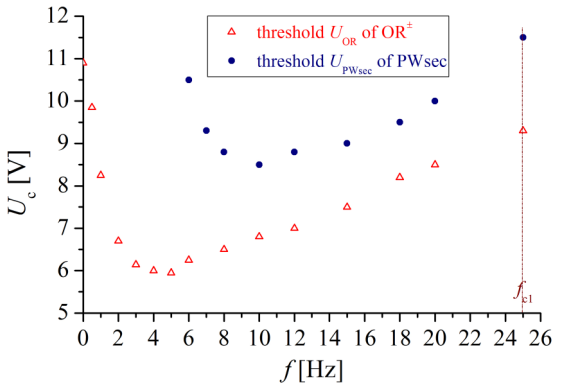

FIG. 4. (Color online) Frequency dependence of the threshold voltages of $OR^\pm$ and PWsec (see text later). The patterns are observed up to the critical frequency f_{c1}. $T = 97\,^\circ$C.

at very low f, as shown in Fig. 4. The steep increase at $f \to 0$ is attributed to the internal voltage attenuation in the cell due to the finite electrical conductivity of the LC. As the capacitive coupling becomes negligible by the reduction of f, screening effects and the voltage drop at the insulating alignment layers become more pronounced [21].

While the direction of the wave vector $\mathbf{q}_{OR}$ alternates with the voltage polarity, the wave number $|\mathbf{q}_{OR}|$ remains about the same within the error limits. Figure 5(a) shows that the dimensionless wave number $q^*_{OR} = |\mathbf{q}_{OR}|d/\pi = 2d/\lambda_{OR}$ (λ_{OR} is the wavelength of the pattern) slightly increases with the frequency, following $U_{OR}(f)$ as usual. The angle $|\alpha_{OR}|$

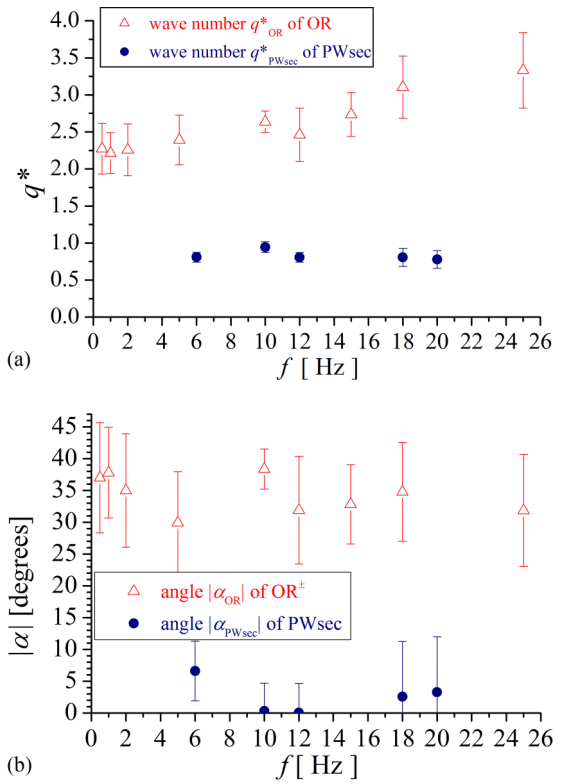

FIG. 5. (Color online) Frequency dependence of (a) the dimensionless wave number $q*$, and (b) the obliqueness angle $|\alpha|$ enclosed by $\mathbf{q}_c$ and $\mathbf{n}_0$ for $OR^\pm$ and PWsec. $T = 97\,^\circ$C.

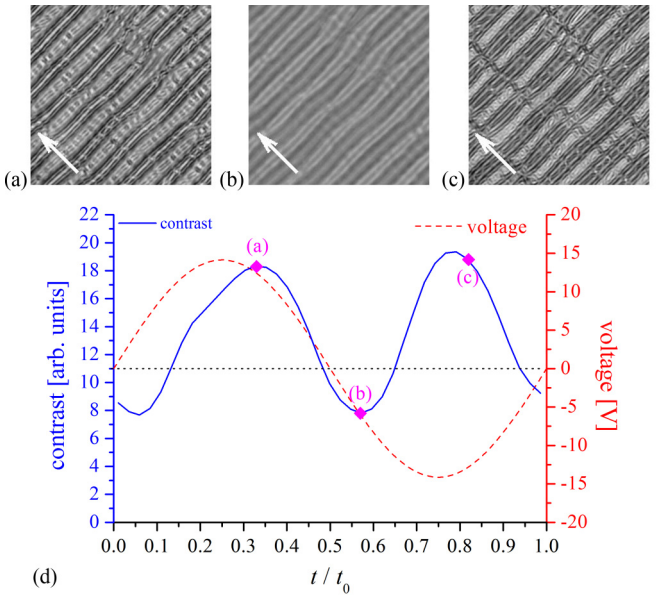

FIG. 6. (Color online) Representative snapshots of the low-frequency ac voltage driven prewavy pattern. (a) PWsec in the positive half period; (b) PWsec around the zero crossing of the voltage; (c) PWsec in the negative half period. All snapshots are of 100 μm × 100 μm size. The white arrows indicate the initial director $\mathbf{n}_0$, the polarizer direction is vertical. (d) Temporal dependence of the pattern contrast and of the applied voltage within one full period. The symbols denote the time instants when the snapshots were taken. $f = 12$ Hz, $U = 10.0$ V, $T = 97\,^{\circ}$C.

between $\mathbf{q}_{\mathrm{OR}}$ and $\mathbf{n}_0$ decreases with increasing f as depicted in Fig. 5(b).

If the ac voltage is increased much above the onset U_{OR} of oblique rolls, another pattern emerges at a second threshold voltage U_{PWsec}, whose f dependence is also shown in Fig. 4. This high-voltage pattern, examples of which are shown in Figs. 6(a)–6(c), we will denote as PWsec, since it resembles the prewavy pattern [5] and occurs as a secondary instability. PWsec has a wave vector $\mathbf{q}_{\mathrm{PWsec}}$, different from that of the oblique rolls both in direction and magnitude. The PWsec stripes are 3–5 times wider than the wavelength of ORs, as follows from Fig. 5(a), and are normal to the initial director $\mathbf{n}_0$. Variation of the contrast with time within one period is plotted in Fig. 6(d). It is seen that though the contrast of PWsec has a $2f$ modulation just as ORs do, in contrast to ORs, its minimum value [corresponding to Fig. 6(b)] is much above the background. It indicates that PWsec does not decay fully, thus it is present in the whole driving period. Inspection of the image sequences recorded with the high-speed camera implies that the stripes of PWsec are not stationary; they exhibit dynamically changing defects and zigzag distortions.

In order to demonstrate how the OR$^{\pm}$ → PWsec transition takes place, time sequences of snapshots are shown in Fig. 7 for increasing the voltage suddenly from $U = 0$ to slightly above the threshold U_{PWsec} of PWsec. It is seen that PWsec nucleates randomly in the OR$^{\pm}$ pattern with a time delay of a few seconds; then it extends to the whole sample. The process requires about 20 s for completion; hence it is quite slow, which is not surprising for a prewavy pattern.

The snapshots in Fig. 8 represent an alternative approach, where the voltage is increased slowly in small (0.1 V) steps, allotting enough time (∼10 s) after each voltage change for pattern stabilization. It is seen that upon increasing the voltage the oblique rolls first lose their polarity sensitivity; for both half periods OR^{+} and OR^{-} superpose forming a zigzag pattern. Then domains of PWsec appear with a sharp boundary typical to a backwards bifurcation and expand to fill the space.

We want to emphasize that, as the above observations clearly show, the PWsec pattern obtained at high voltages is not polarity sensitive; $\mathbf{q}_{\mathrm{c}}$ is the same in both half periods.

B. The middle-frequency range

Above the low-frequency range ($f > f_{\mathrm{c1}}$) there is a frequency gap at about 25–50 Hz, where though EC is present,

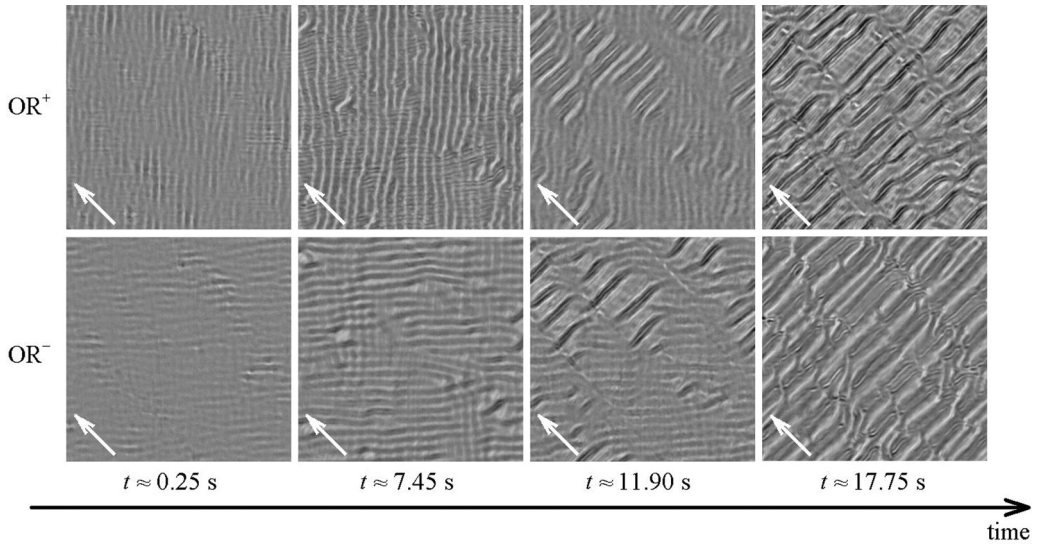

FIG. 7. Transformation of OR$^{\pm}$ into PWsec; a time evolution following a jump of the voltage at $t = 0$ from $U = 0.0$ V $< U_{\mathrm{PWsec}}$ to $U = 10.5$ V $\gtrsim U_{\mathrm{PWsec}}$. The system requires more than $100t_0$ to change from the initial OR$^{\pm}$ to the final PWsec state. $f = 6$ Hz, $T = 97\,^{\circ}$C. All snapshots are of 124 μm × 124 μm size. The white arrows indicate the initial director $\mathbf{n}_0$, the polarizer direction is vertical.

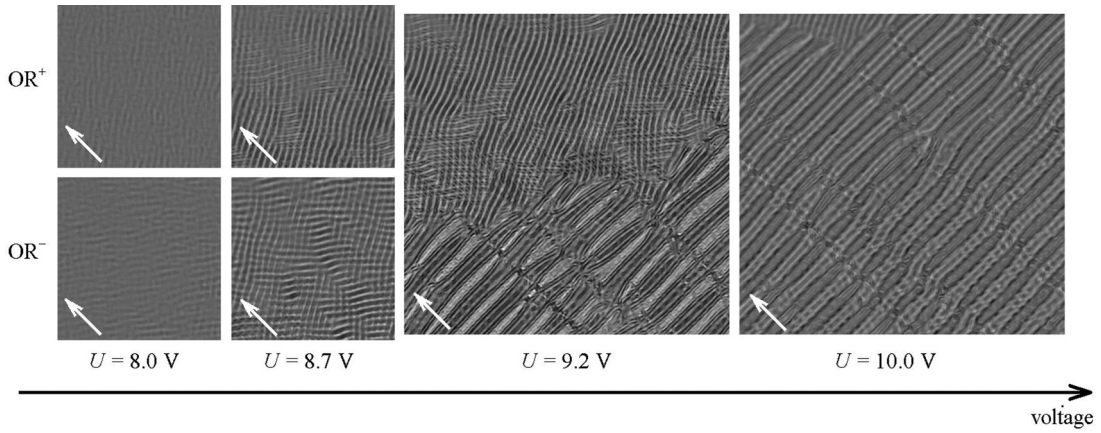

FIG. 8. Transformation of OR$^{\pm}$ into PWsec during gradual, slow voltage increase. $f = 12\,\mathrm{Hz}$, $T = 97\,^{\circ}\mathrm{C}$. The smaller snapshots are of $100\,\mu\mathrm{m} \times 100\,\mu\mathrm{m}$, the bigger ones are of $200\,\mu\mathrm{m} \times 200\,\mu\mathrm{m}$ size. The white arrows indicate the initial director $\mathbf{n}_0$, the polarizer direction is vertical.

no regular stripe patterns associable with a specific wave vector could be observed.

Above this frequency gap, in the middle-frequency range of $50\,\mathrm{Hz} < f < 3\,\mathrm{kHz}$, the characteristics of the patterns are different from those in the low-f range. The rolls are still oblique, forming a zigzag (ZZ) pattern, symmetrical with respect to $\mathbf{n}_0$, at the lower-f part of the range [Fig. 9(a)], but the contrast is rather weak, compared to that of OR$^{\pm}$. Thus for $f > 2\,\mathrm{kHz}$ the wave vector could not be identified. The frequency dependence of the threshold voltage U_{ZZ}, the dimensionless wave number q^*_{ZZ}, and α_{ZZ} of the ZZ pattern are shown in Figs. 10(a)–10(c), respectively.

For the sake of comparison data for the OR$^{\pm}$ pattern were repeated in the figure too. It can be seen that $U_{ZZ}(f)$ is linear, just as $U_{OR}(f)$; however, the two slopes are different and the threshold voltage suffers a jump in the frequency gap between the two types of patterns. The wavelength of ZZ is in the order of d. In contrast to the behavior of OR$^{\pm}$, $\alpha_{ZZ}(f)$ increases monotonically; i.e., the rolls become nearly parallel to $\mathbf{n_0}$ as f is increased, as illustrated in Figs. 9(b) and 9(c).

In order to examine the optical properties of the ZZ pattern, we checked how the shadowgraph contrast depends on the direction of the polarizer. It was found that if the polarizer is either parallel or perpendicular to $\mathbf{n_0}$, the ZZ pattern disappears [the pattern is hardly visible in Figs. 11(a) and 11(b)], whereas the best contrast of the ZZ pattern is obtained at a polarizer position of 45° with respect to $\mathbf{n_0}$ [Fig. 11(c)]. This angular

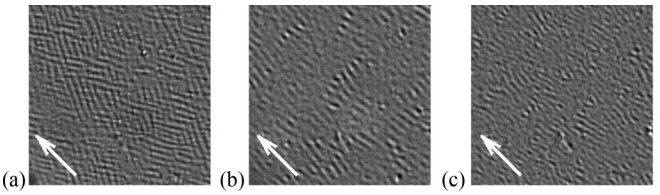

FIG. 9. Representative snapshots of the medium frequency ac voltage driven oblique roll (ZZ) pattern. (a) $f = 50\,\mathrm{Hz}$, $U = 7\,\mathrm{V}$; (b) $f = 1000\,\mathrm{Hz}$, $U = 13\,\mathrm{V}$; (c) $f = 2000\,\mathrm{Hz}$, $U = 20\,\mathrm{V}$. All snapshots are of $100\,\mu\mathrm{m} \times 100\,\mu\mathrm{m}$ size and are strongly contrast enhanced. The white arrows indicate the initial director $\mathbf{n}_0$, the polarizer direction is vertical. $T = 97\,^{\circ}\mathrm{C}$.

dependence clearly demonstrates that the ZZ pattern may involve some twist deformation (azimuthal modulation in the cell plane).

C. The high-frequency range

Finally, in the high-frequency range of $3\,\mathrm{kHz} < f < 80\,\mathrm{kHz}$ the sample exhibits again a different pattern type. It is characterized with wide stripes of wavelength $\Lambda \approx 3d$ which run perpendicular to $\mathbf{n_0}$ (see Fig. 12); this implies that the pattern is also a kind of prewavy pattern [5]. In order to distinguish it from PWsec, we will refer to it as PWprim, since it is the result of a primary instability.

Figures 13(a) and 13(b) show the frequency dependence of the threshold voltage U_{PWprim} and the dimensionless wave number q^*_{PWprim} of PWprim, respectively. It is seen that $U_{PWprim}(f)$ increases monotonically, however, keeping q^*_{PWprim} unaltered. The pattern could not be followed above 80 kHz, as the threshold there rose above the maximal output of our high-voltage amplifier.

Here, we should point out a difference between the two prewavy structures. The PWprim, present in the high-frequency range, is a stationary pattern with high contrast and regular straight rolls. In contrast to that, the PWsec in the low-frequency range, as already mentioned in Sec. III A, has a dynamic character; the stripes are irregular, they are moving, winding, and undulating as time elapses.

D. Measurement of material parameters

Anisotropies of the dielectric permittivity and the electric conductivity are key factors governing the formation and behavior of EC patterns. Therefore we carried out dielectric spectroscopic measurements to determine these parameters. Measurements were performed using planarly aligned, 30.7-μm-thick sandwich cells to obtain the perpendicular components $\varepsilon_\perp$ and $\sigma_\perp$. The parallel components $\varepsilon_\parallel$ and $\sigma_\parallel$ were obtained by reorienting the director by a magnetic field of 1 T, perpendicular to the electrodes. Due to the relatively large resistance of the ITO electrodes, the dielectric properties of 9P-CF_2O-ODBP could be measured reliably only up to 10 kHz. The measurements indicated that the BCN

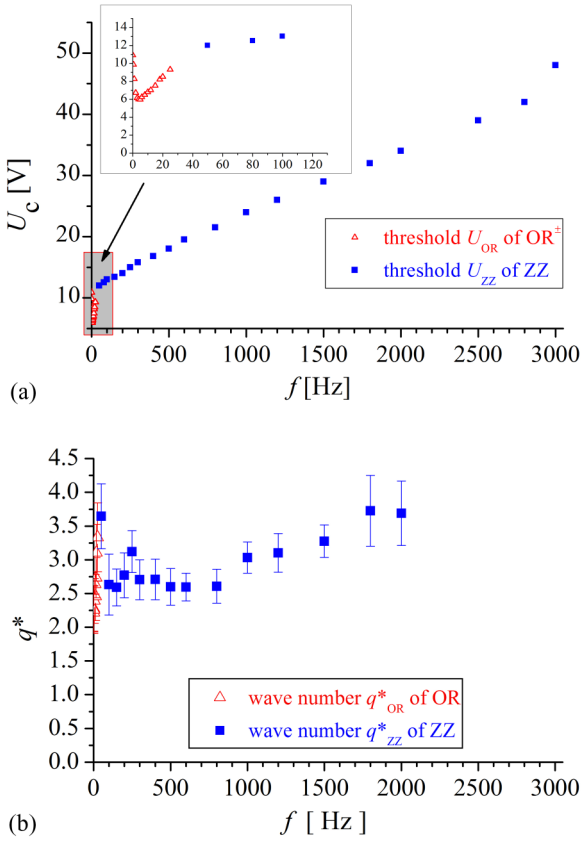

FIG. 10. (Color online) Frequency dependence of (a) the threshold voltages U_c, (b) the dimensionless wave numbers q^* and (c) the angle $|\alpha|$ between the wave vector $\mathbf{q}_c$ and $\mathbf{n}_0$ for the ZZ and the OR$^{\pm}$ patterns. The inset in (a) shows in more detail the neighborhood of the frequency gap 25 Hz < f < 50 Hz, where no regular patterns could be observed. T = 97 °C.

material 9P-CF_2O-ODBP, unlike other bent-core materials [25,26], does not show any dispersion in the 100 Hz–10 kHz frequency range, neither in the perpendicular, nor in the parallel component.

An increase of $\varepsilon_\perp$ and $\varepsilon_\parallel$ below 100 Hz indicated the fairly large electrical conductivity ($\sigma_\perp \sim 10^{-7}$ S m^{-1}) of the compound. We found that the dielectric ($\varepsilon_a = \varepsilon_\perp - \varepsilon_\parallel$) and the conductivity ($\sigma_a = \sigma_\perp - \sigma_\parallel$) anisotropies are negative and nearly constant over the whole considered frequency range (100 Hz–10 kHz).

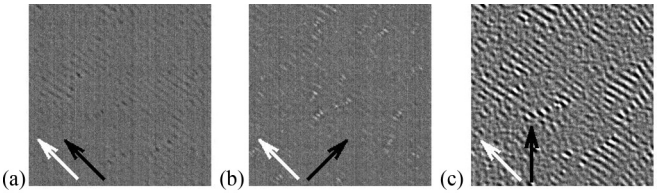

FIG. 11. Snapshots of the ZZ pattern at various polarizer settings. If the polarizer (black arrows) is (a) parallel with or (b) perpendicular to $\mathbf{n}_0$ (white arrows), only a very weak pattern is visible. Maximum pattern contrast is obtained if (c) the polarizer is at 45° to $\mathbf{n}_0$. f = 250 Hz, U = 8 V, T = 97 °C. The images are of 100 μm × 100 μm size.

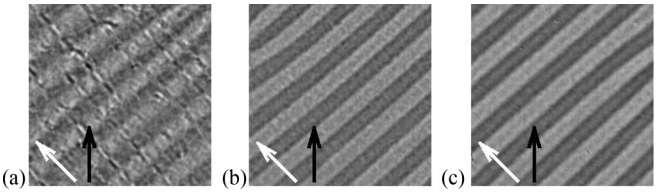

FIG. 12. Representative snapshots of the high-frequency ac voltage driven prewavy (PWprim) pattern. (a) f = 4 kHz, U = 45 V; (b) f = 20 kHz, U = 53 V; (c) f = 70 kHz, U = 82 V. The image sizes are 100 μm × 100 μm. The white arrows indicate the initial director $\mathbf{n_0}$, the black arrows correspond to the polarizer direction.

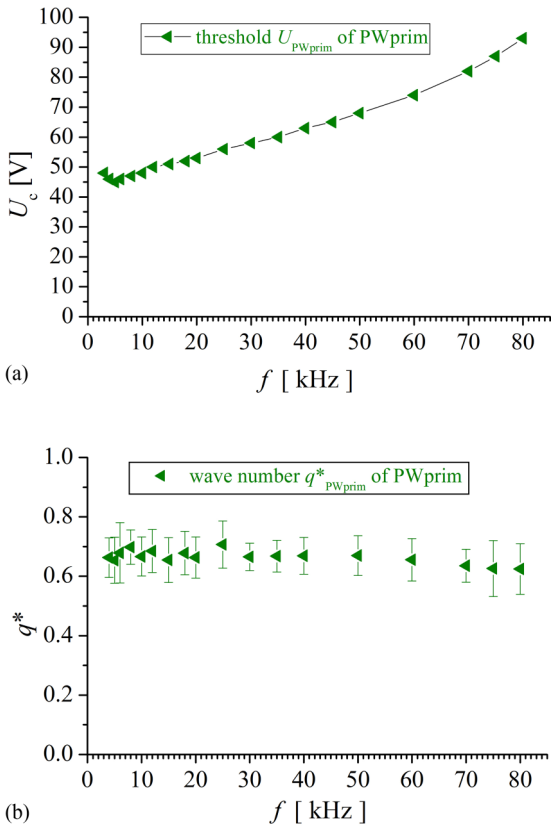

FIG. 13. (Color online) Frequency dependence of (a) the threshold voltage U_c and (b) the dimensionless wave number q^* of the high-frequency prewavy (PWprim) pattern. T = 97 °C.

TABLE I. Material parameters of the BCN compound 9P-CF_2O-ODBP measured at $f = 2$ kHz.

T (deg C)	100	123
K_{11} (pN)	10.65	7.26
K_{22} (pN)	10.59	6.9
K_{33} (pN)	25.6	14.1
χ_a	7.9×10^{-7}	6×10^{-7}
$\varepsilon_\parallel$	5.2	5.72
$\varepsilon_\perp$	9.5	8.49
ε_a	-4.3	-2.8

Monitoring the director reorientation during the electric- and/or magnetic-field-induced splay and twist Fréedericksz transitions by capacitance and optical transmission measurements, further material parameters (the elastic moduli K_{11}, K_{22}, and K_{33} and the anisotropy χ_a of the magnetic susceptibility) could also be measured using a curve fitting procedure [27]. The material parameters obtained at two temperatures are summarized in Table I.

The material parameters of typical BCN compounds differ substantially from those of calamitic ones. BCNs usually exhibit low-frequency dielectric relaxation and have an inverted, $K_{33}/K_{11} < 1$, elastic ratio; their viscosities can be three orders of magnitude higher compared to rodlike compounds [26,28–31]. These special characteristics of typical BCNs are attributed to their bent molecular shape, the resulting preference for a polar ordering and thus the presence of cybotactic smectic clusters [32–36].

Despite its bent molecular structure, the material parameters of 9P-CF_2O-ODBP (listed in Table I) are alike to those of regular rodlike nematic compounds. The lack of low-frequency dielectric relaxation, and the regular, $K_{33}/K_{11} > 1$, elastic ratio corroborate this statement. Furthermore, the viscosity of 9P-CF_2O-ODBP, estimated from the filling time of sandwich cells, was also found to be much lower than that of typical BCN liquid crystals; while 9P-CF_2O-ODBP could be filled in a 30-μm-thick cell in less than 1 min, filling with a typical BCN requires at least 15 min for the same type of cell. Our findings thus indicate that cybotactic clusters are not significantly present in 9P-CF_2O-ODBP. We attribute this to a lower bend angle due to the pentagon shaped central ring that might decrease the tendency of the formation of layered molecular clusters.

We note that the lack of bent-core specialties (like cybotacticity, anomalous elasticity, etc.) in another bent-shaped compound has already been reported and was also explained by molecular structural reasons [37].

IV. DISCUSSION AND CONCLUSIONS

The results above represent an in-depth exploration of electrically induced patterns and the transitions between them in a wide frequency and voltage range. As the tested BCN material exhibits both negative dielectric anisotropy and negative conductivity anisotropy in the whole studied frequency range, the standard Carr-Helfrich mechanism cannot destabilize the initial homogeneous state; consequently all observed patterns belong to nonstandard EC scenarios, just as found in other BCN compounds. It has to be noted, however, that the scenarios exhibited by the 9P-CF_2O-ODBP, and/or their sequence upon alteration of voltage or frequency differ in a large extent from the previously reported ones.

The most interesting, but on the other hand surprising, result is that in the low-frequency range ($0 < f < 25$ Hz) the pattern (OR^+ and OR^-) is polarity sensitive; the wave vectors appear alternatingly in the positive and negative half cycles of the driving voltage, respectively. OR^+ and OR^- correspond to the two degenerate solutions of the oblique rolls morphology. The oblique rolls observed earlier (whether in standard or in nonstandard EC) did not exhibit a similar effect; the two solutions were either superposed forming a grid pattern or coexisted in zigzag domains. It is a challenging task to find out how and why in 9P-CF_2O-ODBP the polarity of the voltage distinguishes between the solutions, breaking their degeneracy.

Flexoelectricity should play a key role, since the flexoelectric torque $\Gamma_{\mathbf{p}} = \mathbf{P}_{\mathrm{fl}} \times \mathbf{E}$ is the only one linear in the electric field; the dielectric torque is quadratic ($\propto \mathbf{E}^2$), while the elastic and viscous ones do not depend on $\mathbf{E}$. Indeed, polarity-dependent deformations have been reported in geometries where the flexoelectric interaction dominates over the dielectric one [38]. The flexoelectric response may be especially important in asymmetrical cells where the top and bottom surfaces differ in the orientation directions (e.g., hybrid aligned cells [39–41]), or in the anchoring strength [42,43], its anisotropy, or in ionic adsorption. The polarity sensitive response then mostly manifests itself in different thresholds at positive and negative voltages [40–43].

Patterns with polarity sensitive wave vector have so far been reported only in the twisted planar geometry [44–46], where the alignment directions at the two surfaces made a large (90° or 18°) angle with each other. The pattern formation (whether electroconvection or flexoelectric domains) was there interpreted as surface driven, occurring always near the cathode; hence $\mathbf{q}$ was determined by the alignment at that surface. As a consequence, the angle of rotation of $\mathbf{q}$ upon reversal of the polarity of the applied voltage was in correlation with the twist angle of the cell.

We have to emphasize, however, that in our planar cell the twist angle is (nominally) zero; thus this surface mechanism (which has also not been fully understood yet) would yield the same $\mathbf{q}$ for both polarities. In contrast to that, our findings indicate a so far unprecedented polarity sensitive selection of the wave vector from among two degenerate directions and also imply that in our case the pattern formation has a bulk mechanism, rather than a surface one.

Actually, 9P-CF_2O-ODBP is a bent-core nematic which, due to the combination of its bent molecular structure with the transverse component of its dipole moment, is an ideal candidate for a large flexoelectric response. If this is coupled with an (accidental and small) wedge shape, pretilt, and/or pretwist (which distinguishes a real planar cell from an ideal one), then a symmetry breaking of the solution might occur [47]. It is also a remarkable coincidence that the polarity sensitive pattern occurs in that low-frequency range where ionic migration and adsorption and desorption effects may be significant too.

Though the measurements were extended to very high frequencies and prewavy patterns could be observed up to 80 kHz,

the special scenario with negative slope of dV_c/df could not be found in 9P-CF_2O-ODBP. It is yet unclear and is a task for future investigations, whether the lack of this scenario is in correlation with the missing cybotacticity of the compound.

The behavior of 9P-CF_2O-ODBP differs also from that of the shorter members (8P-CF_2O-ODBP [19] and 7P-CF_2O-ODBP [48]) of the same homologous series. Though this might be surprising at first sight, it is not unprecedented. Significant changes in the pattern forming behavior induced by a little alteration of the length of the end chains of calamitic molecules have already been reported for electric-field-induced [49] as well as for solidification [50] patterns.

ACKNOWLEDGMENTS

The authors are thankful to Zhi-Yong Zhang (Wuhan Polytechnic University) for providing the compound studied and to Alexei Krekhov for fruitful discussions. This work was supported by the National Natural Science Foundation of China (Grants No. 11374067 and No. 11074054), the Hungarian Scientific Research Fund (OTKA) (Grant No. NN110672), and the Inter-Governmental S&T Cooperation Proposal Between Hungary and China (6-8 "Complex study of nonlinear structures in novel types of liquid crystals," TÉT_12_CN-1-2012-0039).

[1] L. Kramer and W. Pesch, in *Pattern Formation in Liquid Crystals*, edited by A. Buka and L. Kramer (Springer, Berlin, 1996), pp. 221–255.
[2] Á. Buka, N. Éber, W. Pesch, and L. Kramer, in *Self Assembly, Pattern Formation and Growth Phenomena in Nano-Systems*, edited by A. A. Golovin and A. A. Nepomnyashchy (Springer, Dordrecht, 2006), pp. 55–82.
[3] E. Bodenschatz, W. Zimmermann, and L. Kramer, J. Phys. (Paris) **49**, 1875 (1988).
[4] A. Krekhov, W. Pesch, N. Éber, T. Tóth-Katona, and Á. Buka, Phys. Rev. E **77**, 021705 (2008).
[5] J.-H. Huh, Y. Hidaka, Y. Yusril, N. Éber, T. Tóth-Katona, Á. Buka, and S. Kai, Mol. Cryst. Liq. Cryst. **364**, 111 (2001).
[6] H. Takezoe and Y. Takanishi, Jpn. J. Appl. Phys. **45**, 597 (2006).
[7] D.Wiant, J. T. Gleeson, N. Éber, K. Fodor-Csorba, A. Jákli, and T. Tóth-Katona, Phys. Rev. E **72**, 041712 (2005).
[8] R. Stannarius and J. Heuer, Eur. Phys. J. E **24**, 27 (2007).
[9] J. Heuer, R. Stannarius, M.-G. Tamba, and W. Weissflog, Phys. Rev. E **77**, 056206 (2008).
[10] P. Kumar, U. S. Hiremath, C. V. Yelamaggad, A. G. Rossberg, and K. S. Krishnamurthy, J. Phys. Chem. B **112**, 9753 (2008).
[11] S. Tanaka, S. Dhara, B. K. Sadashiva, Y. Shimbo, Y. Takanishi, F. Araoka, K. Ishikawa, and H. Takezoe, Phys. Rev. E **77**, 041708 (2008).
[12] S. Tanaka, H. Takezoe, N. Éber, K. Fodor-Csorba, A. Vajda, and Á. Buka, Phys. Rev. E **80**, 021702 (2009).
[13] P. Tadapatri, K. S. Krishnamurthy, and W.Weissflog, Phys. Rev. E **82**, 031706 (2010).
[14] P. Tadapatri, U. S. Hiremath, C. V. Yelamaggad, and K. S. Krishnamurthy, J. Phys. Chem. B **114**, 10 (2010).
[15] P. Tadapatri and K. S. Krishnamurthy, J. Phys. Chem. B **116**, 782 (2012).
[16] Y. Xiang, J. W. Goodby, V. Gortz, and H. F. Gleeson, Appl. Phys. Lett. **94**, 193507 (2009).
[17] S. Kaur, A. Belaissaoui, J. W. Goodby, V. Gortz, and H. F. Gleeson, Phys. Rev. E **83**, 041704 (2011).
[18] P. Tadapatri, K. S. Krishnamurthy, and W. Weissflog, Soft Matter **8**, 1202 (2012).
[19] Y. Xiang, Y.-K. Liu, Á. Buka, N. Éber, Z.-Y. Zhang, M.-Y. Xu, and E. Wang, Phys. Rev. E **89**, 012502 (2014).
[20] K. S. Krishnamurthy, P. Tadapatri, and P. Viswanath, Soft Matter **10**, 7316 (2014).
[21] N. Éber, L. O. Palomares, P. Salamon, A. Krekhov, and Á. Buka, Phys. Rev. E **86**, 021702 (2012).
[22] P. Salamon, N. Éber, A. Krekhov, and Á. Buka, Phys. Rev. E **87**, 032505 (2013).
[23] T. J. Dingemans and E. T. Samulski, Liq. Cryst., **27**, 131 (2000).
[24] Polyimide KPI200 from Shenzhen Kelead Photoelectronic Materials Co., Ltd, China, was used.
[25] P. Salamon, N. Éber, Á. Buka, J. T. Gleeson, S. Sprunt, and A. Jákli, Phys. Rev. E, **81**, 031711 (2010).
[26] P. Tadapatri, U. Hiremath, C. Yelamaggad, and K. Krishnamurthy, J. Phys. Chem. B **114**, 1745 (2010).
[27] M. Majumdar, P. Salamon, A. Jákli, J. T. Gleeson, and S. Sprunt, Phys. Rev. E **83**, 031701 (2011).
[28] P. Sathyanarayana, B. Sadashiva, and S. Dhara, Soft Matter **7**, 8556 (2011).
[29] Á. Buka, N. Éber, K. Fodor-Csorba, A. Jákli, and P. Salamon, Phase Transitions **85**, 872 (2012).
[30] N. Avci, V. Borshch, D. D. Sarkar, R. Deb, G. Venkatesh, T. Turiv, S. V. Shiyanovskii, N. V. S. Rao, and O. D. Lavrentovich, Soft Matter **9**, 1066 (2013).
[31] A. Chakraborty, M. K. Das, B. Das, A. Lehmann, and C. Tschierske, Soft Matter **9**, 4273 (2013).
[32] S. Hong, R. Verduzco, J. Williams, R. Twieg, E. Dimasi, R. Pindak, A. Jákli, J. Gleeson, and S. Sprunt, Soft Matter **6**, 4819 (2010).
[33] S. H. Hong, R. Verduzco, J. T. Gleeson, S. Sprunt, and A. Jákli, Phys. Rev. E **83**, 061702 (2011).
[34] C. Zhang, M. Gao, N. Diorio, W. Weissflog, U. Baumeister, S. Sprunt, J. T. Gleeson, and A. Jakli, Phys. Rev. Lett. **109**, 107802 (2012).
[35] S. Chakraborty, J. T. Gleeson, A. Jakli, and S. Sprunt, Soft Matter **9**, 1817 (2013).
[36] O. Francescangeli, F. Vita, and E. T. Samulski, Soft Matter **10**, 7685 (2014).
[37] P. Salamon, N. Éber, J. Seltmann, M. Lehmann, J. T. Gleeson, S. Sprunt, and A. Jákli, Phys. Rev. E **85**, 061704 (2012).
[38] N. V. Madhusudana, in *Flexoelectricity in Liquid Crystals. Theory, Experiments and Applications*, edited by Á. Buka and N. Éber (Imperial College Press, London, 2012), pp. 33–60.
[39] I. Dozov, Ph. Martinot-Lagarde, and G. Durand, J. Phys. Lett. **43**, 365 (1982).
[40] N. V. Madhusudana and G. Durand, J. Phys. Lett. **46**, 195 (1985).
[41] B. Valenti, C. Bertoni, G. Barbero, P. Taverna-Valabrega, and R. Bartolino, Mol. Cryst. Liq. Cryst. **146**, 307 (1987).
[42] W. Helfrich, Appl. Phys. Lett. **24**, 451 (1974).

[43] Y. Marinov, H. P. Hinov, and A. G. Petrov, J. Optoelectron. Adv. Mater. **7**, 277 (2005).
[44] K. S. Krishnamurthy, P. Kumar, and M. V. Kumar, Phys. Rev. E **87**, 022504 (2013).
[45] K. S. Krishnamurthy, Phys. Rev. E **89**, 052508 (2014).
[46] O. Elamain, Ph.D. thesis, University of Gothenburg, 2013.
[47] A. Krekhov (private communication).
[48] Y. Xiang *et al.* (unpublished).
[49] E. Kochowska, Sz. Németh, G. Pelzl, and Á. Buka, Phys. Rev. E **70**, 011711 (2004).
[50] T. Tóth-Katona, T. Börzsönyi, Z. Váradi, J. Szabon, Á. Buka, R. González-Cinca, L. Ramírez-Piscina, J. Casademunt, and A. Hernández-Machado, Phys. Rev. E **54**, 1574 (1996).